Pressure pushes $tRNA^{Lys3}$ into excited conformational states

Jinqiu Wang[1], Tejaswi Koduru[2], Balasubramanian Harish[2*], Scott A. McCallum[3], Kevin P. Larsen[4,#], Karishma S. Patel[4,&], Edgar V. Peters[5], Richard E. Gillilan[6], Elisabetta V. Puglisi[4], Joseph D. Puglisi[4], George Makhatadze[2] and Catherine A. Royer[2‡]

[1] Graduate Program in Biochemistry and Biophysics, Rensselaer Polytechnic Institute, Troy , NY 12180

[2]Department of Biological Sciences, Rensselaer Polytechnic Institute, Troy , NY 12180

[3]Center for Biotechnology and Interdisciplinary Studies, Rensselaer Polytechnic Institute, Troy NY 12180

[4]Department of Structural Biology, Stanford University School of Medicine, Stanford, CA 94305

[5]Department of Chemistry and Chemical Biology, Rensselaer Polytechnic Institute, Troy NY 12180

[6]Cornell High Energy Synchrotron Source, Cornell University, Ithaca, NY 14853

*Current address - Department of Physical Chemistry, Faculty of Chemistry and Chemical Biology, Technical University of Dortmund, Dortmund Germany 44227

#Current address - Department of Molecular & Cell Biology, University of California, Berkeley, Berkeley, CA 94720

&Current address - University of Massachusetts Chan Medical School, T.H. Chan School of Medicine, Worcester, MA 01605

‡ - To whom correspondence should be addressed

Author Contributions

Jinqiu Wang – produced and purified tRNA, acquired and analyzed high pressure NMR data, acquired and analyzed high pressure SAXS data, wrote the manuscript

Tejaswi Koduru – carried out EOM modeling of RNA conformations, wrote the manuscript

Balasubramanian Harish – Assisted in tRNA production and NMR and SAXS data acquisition

Scott A. McCallum – Assisted in tRNA NMR data acquisition and analysis, wrote the paper

Kevin P. Larsen – Assisted in tRNA production

Karishma A. Patel – Assisted in tRNA production

Edgar V. Peters – Assisted in additional NMR data analysis

Richard E. Gillilan – Assisted in high pressure SAXS data acquisition and analysis

Elisabetta V. Puglisi. Contributed to tRNA NMR and sample production

Joseph D. Puglisi – Contributed to conception of study, assisted in setting up tRNA production, participated in tRNA production troubleshooting, interpreted NMR results, wrote the manuscript

George Makhatadze – Suggested and carried out structure-based modeling of tRNA

Catherine A. Royer – Conceived the project, oversaw the project, analyzed and interpreted results, wrote the manuscript

Competing Interest Statement: None.

Classification: Physical Sciences, Biophysics and Computational Biology

Biological Sciences, Biophysics and Computational Biology

Keywords: RNA, high pressure, NMR, SAXS, molecular dynamics simulations.

Abstract

Conformational dynamics play essential roles in RNA function. However, detailed structural characterization of excited states of RNA remains challenging. Here we apply high hydrostatic pressure (HP) to populate excited conformational states of $tRNA^{Lys3}$, and structurally characterize them using a combination of HP 2D-NMR, HP-SAXS and computational modeling. HP-NMR revealed that pressure disrupts the interactions of the imino protons of the uridine and guanosine U-A and G-C base pairs of $tRNA^{Lys3}$. HP-SAXS profiles showed a change in shape, but no change in overall extension of the tRNA at HP. Configurations extracted from computational ensemble modeling of HP-SAXS profiles were consistent with the NMR results, exhibiting significant disruptions to the acceptor stem, the anticodon stem and the D-stem regions at HP. We propose that initiation of reverse transcription of HIV RNA could make use of one or more of these excited states.

Significance Statement

Conformational dynamics and high energy excited states play important roles in RNA function, underscoring the importance of their detailed structural and energetic characterization. High pressure perturbation leads to an increase in the population of RNA excited states. Combining high pressure, 2D-NMR, SAXS and computation allowed evaluation of the stability and structural properties of excited states of human $tRNA^{Lys3}$.

Introduction

RNA molecules populate highly dynamical ensembles undergoing structural interconversions on multiple timescales (*e.g.,* (1–8)). These RNA conformational ensembles and dynamic transitions between conformational states play a central role in RNA function (9). Indeed, single nucleotide polymorphisms and insertions in RNA molecules have been shown to cause changes in RNA structural ensembles that are linked to disease states (10–14). Coupling of secondary structure and tertiary interactions in $tRNA^{Phe}$ appear to control conformational dynamics and the cooperativity of folding (15). Stability of the D-stem in yeast $tRNA^{Asp}$ was shown to significantly modulate the specificity constant for aspartylation by aspartyl tRNA synthetase (16), and tRNA dynamics influence appropriate tRNA selection by the ribosome (17). Moreover, retroviruses employ cellular tRNA molecules as primers in the reverse transcription of their viral genomes (18), a process which requires a large conformational change in the tRNA. In particular, the human immunodeficiency virus (HIV) uses cellular $tRNA^{Lys3}$, the object of the present study, as a reverse transcription primer.

The structural and dynamic properties of RNA ensembles and linkage to function have been extensively investigated. Nuclear magnetic resonance (NMR) approaches have provided significant insight (*e.g.*, (1–4, 19)). Förster Resonance Energy Transfer (FRET), particularly in single molecule mode, has also yielded important dynamic information about RNA conformational transitions (*e.g.*, (17, 20–25)). Other fluorescence methods, small angle x-ray scattering (SAXS) and computational approaches have also been used to detect and characterize RNA conformational changes (*e.g.,* (8, 26–32)).

The most functionally relevant forms of RNA in the conformational ensembles often correspond to high-energy, poorly-populated excited states. Detecting and characterizing such states experimentally pose significant challenges. In addition to single-molecule FRET, NMR relaxation dispersion is a highly useful approach to this problem (33), which, nonetheless, requires that the excited states of interest be populated at a level of ~2% or more. Magnesium ion depletion or heating both lead to partial or complete RNA unfolding, but these are rather harsh treatments that are not always reversible. High hydrostatic pressure (HP) represents a more gentle, continuous and generally reversible perturbation which can in principle favor high energy excited states of RNA. Excited states of biomolecules generally occupy smaller molar volumes, and are thus favored by pressure (34, 35). However, in contrast to the extensive literature concerning pressure effects on protein conformation, few studies on HP effects on RNA have been appeared to date (36–45). These studies have shown that the structures of RNA tetraloops (38), hairpins (39), G-quadruplex aptamers (40), ribozymes (42, 43) and tRNA (41, 44, 45) are disrupted at high pressure.

Here we characterize post-transcriptionally unmodified, *in vitro* transcribed, human $tRNA^{Lys3}$, (Figure 1A) using a combination of two-dimensional HP-NMR and HP-SAXS, coupled with computational approaches. HP-NMR revealed that pressure disrupts the interactions of the hydrogen-bonded imino protons of the uridine and guanosine U-A and G-C base pairs, of $tRNA^{Lys3}$, with associated volume changes of approximately ~20 ml/mol for the folding transitions at low $MgCl_2$ concentration. The pressure midpoints for the transitions were Mg^{2+} ion-dependent, as expected. HP-SAXS at 1 mM $MgCl_2$ revealed that while HP did not result in significant change in the global extension of the molecule, the shape of $tRNA^{Lys3}$ was clearly perturbed at 3 kbar. Temperature-dependent structure-based modeling (SBM) (46) produced a large ensemble of $tRNA^{Lys3}$ structures, sub-ensembles of which were used to select configurations consistent with the experimental SAXS profiles using the Ensemble Optimization Method (EOM)(47). At low pressure, three configurations with 0.98-1.0 fractional native contacts relative to the crystal structure of native $tRNA^{Lys3}$ (48) (Fig.1) were sufficient to describe the SAXS profile, and exhibited only slight differences in orientation of the anticodon loop and acceptor stem. In contrast, at 3 kbar the EOM-selected structures exhibited strong disruption in the acceptor stem,

the region which serves as the primer for HIV reverse transcription in addition to perturbations to the D-stem/loop and anticodon stem/loop regions. We suggest that these excited state configurations represent sparsely populated states that can be exploited by the invading viral RNA to initiate HIV reverse transcription.

Results

HP populates tRNA^{Lys3}states with decreased base-pair stability

We sought to determine whether pressure modified the conformation of tRNA^{Lys3} by observation of the pressure dependence of the ^{1}H-^{15}N HSQC spectrum in the imino proton region of ^{15}N-labeled tRNA^{Lys3} labeled at U and G bases produced by *in vitro* transcription (49, 50) at pH 6.5. The spectrum was identical to that previously reported (Fig 1A-D, blue, (49)). The imino protons of the base-paired guanosine and uridine bases of tRNA^{Lys3} have been assigned (51), and along with 2D proton NOE experiments, have shown that its structure is consistent with the expected conformation (48), although somewhat less stable (51, 52). All of the previously detected base paired imino protons were detected in the ^{1}H-^{15}N HSQC obtained at 1 mM $MgCl_2$, pH 6.5 (Figure 1 C –F). Note the upfield shifted resonances for the U55 imino proton which is not base paired (Figure 1B). Rather, it is found in the T-loop, and hence is somewhat shielded from solvent. The imino protons for G6 and U67 are also shifted upfield. These bases are found in a GoU wobble base pair (Figure 1B). Since lowering pH can result in increased peak intensity due to slower solvent exchange, we also measured the spectrum at pH 5.5 (53). The spectrum obtained at lower pH in presence of 1 mM MgCl2 was nearly identical to that at pH 6.5 (Figure S1). All of the base paired residues at pH 6.5 were present at pH 5.5, with the exception of U55. We note as well the presence of an additional peak at pH 5.5 (13.4 ppM ^{1}H and 162.5 ppm ^{15}N), perhaps that of U66, which was not detected in the original structural study of tRNA^{Lys3} (51). While the appearance of the new peak likely arises from slower solvent exchange, the loss of the U55 imino proton peak is likely due to pH dependent changes in the tRNA structure, leading to greater solvent accessibility of the unpaired U55 in the T-loop.

Pressure significantly modified the imino proton 2D ^{1}H-^{15}N HSQC spectrum of tRNA^{Lys3} at 1 mM $MgCl_2$ and pH 6.5 (Figure 1C, D). We note that, although all base-paired guanosine imino proton resonances were detected at atmospheric pressure, several could not be quantified as a function of pressure due to peak overlap. First, as expected, peaks shifted due to compression. The larger shifts of the uridine peaks, as compared to the guanosine peaks suggest higher compressibility for A▪U as compared to G▪C base pairs, perhaps arising from the their difference in stability. More strikingly, the intensity of both the guanosine and uridine imino proton peaks decreased significantly with pressure between 10 and 3000 bar under these conditions (Figure 1G). This decrease in intensity was reversible (Figure S2) and was inhibited by increasing the $MgCl_2$ concentration to 20 mM (Figure 2A-F, Figures S3, S4). To examine whether the pressure dependence of the HSQC peak intensities was pH-dependent, we carried out the pressure dependent HSQC measurements at pH 5.5. The pressure-dependence of the imino proton intensities at lower pH were similar or slightly less pressure-resistant compared the results at pH 6.5 for those imino protons that could be quantified as a function of pressure under both conditions (Figure S5).

Imino protons of RNA base pairs (N3U and N1G) exchange with solvent in a two-step process involving an equilibrium between the closed and opened forms of the base pair, followed by exchange exclusively from the open form. Unless they are protected from solvent in tight loops, non-H-bonded imino protons are difficult to detect because their exchange with solvent is fast on the NMR timescale. Base pair closing rates are in the range of 10^{8} s^{-1} (53). Since the catalytic step is always much slower than closing, regardless of conditions, exchange from the open base pair is limiting for the exchange reaction in an EX2 mechanism. At pH 6.5 and below, rather than being

directly catalyzed by water or H+ ions, base-paired U imino protons exchange via intrinsic catalysis by the N1 of the complementary A, while the acid-induced exchange of the G imino protons occurs via the pH-dependent fraction of N7-protonated guanosine (53, 54). Upon physical or chemical perturbation, and in the absence of any changes in the catalytic step, changes in overall exchange rates, and hence peak intensity, reflect changes in the thermodynamic stability of the base pairs. The step in which the imino proton of the open base pair is exchanged with solvent is unlikely to be pressure dependent since the internal mechanism involves groups with pKa ~4 (53, 54), and moreover, like similar chemical moieties, should exhibit small pressure dependence (55).

The pressure-dependent intensity profiles of the imino proton peaks of the uridine and guanosine bases that could be quantified as a function of pressure at pH 6.5 and 1 mM $MgCl_2$ were fit individually to 2-state transitions between folded and excited state (Figure 1G), as described in the Methods section. These transitions are locally 2-state because the imino proton is either in its native state or it is not. Given the indirect mechanism of exchange involving the nitrogen of the complementary base in the pair, pressure is unlikely to increase the rate of the exchange of the imino proton of the open base pair. Thus, the loss of imino proton peak intensity with pressure can be interpreted as a pressure-induced change in RNA conformation that lowers the stability of its base pairs. The recovered free energy values at atmospheric pressure for the transitions at 1 mM $MgCl_2$ were mostly ~1 kcal/mol (Table S1), while the volume change associated with the transition was ~-20 mL/mol. The small variability in the recovered free energy values for most of the imino protons is consistent with a concerted pressure-induced transition involving most base pairs. The transitions for the imino protons at G30, G69 and interestingly, the non-base paired U55, yielded slightly higher free energy value than the others (~1.5 kcal/mol), consistent with deviation from global 2-state behavior for the transition. Free energy changes extrapolated to atmospheric pressure of 1-1.4 kcal/mol are small compared to those derived from the opening free energies derived from base pair lifetime measurements (3-10 kcal/mol). Thus, the transition is not from an H-bonded state for all base pairs to a non H-bonded state, but rather from the native state to a state with lower H-bond stability, presumably due to an increase in the opening rate. By 3000 bar, this excited state (or these excited states) is favored over the native state by ~3 kcal/mol. Volume changes for RNA structural transitions result from a combination of changes in hydration, ion interactions and loss of internal cavities (56). Despite the significant loss in imino proton peak intensity for all of the detected uridine and guanosine bases, the modest values of the volume and free energy changes observed here for the $tRNA^{Lys3}$ pressure-induced transition (roughly equivalent to the molar volume of a single water molecule) indicate rather subtle effects of pressure on $tRNA^{Lys3}$ structure.

The intensity vs pressure profiles obtained at pH 6.5 were clearly shifted to higher pressures with increasing $MgCl_2$ concentration (Figure 2, Figures S4 & S5), consistent with the interpretation that the pressure dependence of the imino peak intensity reflects a transition to a state with lower base pair stabilities and is disfavored by Mg^{2+} ions. Because the changes in imino proton peak intensity at 20 mM $MgCl_2$ were small, the thermodynamic parameters recovered from fits of these data were less reliable (Table S1). However, while some imino peaks show negligible loss in intensity at 20 mM $MgCl_2$ (Figure 2A-D), those of U8 and U12 are visibly less pressure resistant, even at high $MgCl_2$ (Figure 2E,F). For other imino protons, the negligible pressure effects on imino peak intensity at high Mg^{2+} concentration arise from strong local stabilization against pressure perturbation by the divalent cation. Imino proton peaks exhibiting the most pronounced pressure resistance at high $MglC_2$ concentration (G5, G42, G52 and U64) are found near the positions of the crystallographically determined Mg^{2+} and Na^{+} ions in the structure of the native (modified) molecule (Figure 2G) (48). The fact that increasing $MgCl_2$ leads to pressure resistance of the loss of imino proton peak intensity supports the conclusion that pressure leads to the population of a state (or states) with lower base pair stability.

HP alters the global shape of tRNA^{Lys3}

The HP 2D NMR of tRNA^{Lys3} indicated a loss of H-bonding of the imino proton-containing base pairs with increasing pressure, but the extent of the structural disruption could not be determined from these observations alone. Indeed, the observed loss of imino proton peak intensity could arise from pressure-induced dynamics between base-paired and unpaired configurations without significant global unfolding of the tRNA structure. HP ^{1}H-^{1}H NOE experiments were not feasible given the decreased sensitivity in the ceramic HP cell. To gain a deeper understanding of the effects of HP on the global structure of tRNA^{Lys3}, HP SAXS experiments were performed at a $MgCl_2$ concentration of 1 mM. Under these conditions, significant loss of imino proton intensity was observed for most bases over our available pressure range.

From the SAXS intensity profiles at 10 bar and 3000 bar, the pair distribution profiles were computed by inverse Fourier transform (Figure 3A, B). The P(r) distribution at 10 bar was smooth with a peak at ~20 Å and a maximum distance between scattering centers, D_{max}, of ~75 Å, consistent with a folded tRNA structure. While the D_{max} showed no change at HP, the shape of the P(r) distribution was perturbed significantly, with a clear secondary peak appearing at ~35 Å. Likewise, the normalized Kratky plot (Figure 3C) exhibited a shift to slightly higher qR_g values. A small, but significant (~0.5 Å) pressure-dependent increase in the radius of gyration, R_g, was also observed (Figure 3D). These results are consistent with a HP-induced change in shape of the tRNA.

Excited state structures of tRNA^{Lys3} deduced from ensemble optimization

The Ensemble Optimization Method (EOM) has been used to successfully model underlying protein conformational ensembles that give rise to SAXS profiles (*e.g.* (57–60)). Recently, studies of the application of EOM to characterize RNA conformational ensembles have appeared as well (61, 62). Here, all-atom Replica-Exchange Structure-Based Modeling (RESBM) (46, 63) and the crystal structure of modified, natural tRNA^{Lys3} (48) were used to generate a large ensemble of increasingly disrupted structures of tRNA^{Lys3} from fully native to completely unfolded configurations. This large conformational ensemble was subdivided into configurational sub-ensembles of decreasing Q-value (Q = fraction of native contacts). Next, the most probable configurations giving rise to the observed SAXS results at 10 and 3000 bar were identified by EOM analysis. Three configurations from the sub-ensemble representing 0.98-1.0 fractional native contacts were sufficient for excellent reproduction of the SAXS profile obtained at 10 bar (Figure 4), and corresponded to the lowest χ^2 value obtained from the EOM modeling ,(Figure S6). Both the intensity profile and the P(r) plot were recapitulated by three structures, at 44, 33 and 22% population, respectively. The structures were nearly identical, exhibiting only small differences in the orientation of the anti-codon loop and the extreme terminus of the acceptor stem (Figure S7A).

At 3000 bar, five configurations from the ensemble exhibiting 0.84-0.86 fractional native contacts described best the SAXS profile obtained under these conditions (Figure 5). The five recovered structures at 58, 17, 8, 8 and 8% relative population respectively, recapitulated both the SAXS intensity and P(r) profiles at 3000 bar. EOM analysis of lower and higher Q sub-ensembles yielded higher χ^2 values (Figure S6). In contrast to the structures obtained from EOM of the SAXS data at low pressure, the HP configurations recovered from EOM analysis of the 0.84-0.84 Q sub-ensemble were much more disrupted (compare Figures 6 and 7, Figure S7). In particular, the area surrounding the junction between the acceptor stem and the T-loop was significantly perturbed in the HP states, along with lower probability disruptions of the acceptor stem itself. Some perturbation of the anti-codon and D-stem structures was also observed, with a widening of the D-stem and the top of the anti-codon stem in some of the configurations (Fig 5 E,F). Moreover,

the different regions of the $tRNA^{Lys3}$, in particular the acceptor stem and anticodon, T and D loops, were reoriented with respect to each other (Fig 5, E-G), consistent with the clear change in shape apparent in the P(r) plot at high pressure.

Conclusions

The combination of 2D ^{1}H-^{15}N HSQC NMR and SAXS have revealed that HP leads to the population of low-lying excited states of unmodified $tRNA^{Lys3}$. These excited states clearly exhibit lower base-pair stability and changes in shape arising from relative re-orientation of the stem loop structures. At 1 mM Mg^{2+}, these excited states lie ~1-1.5 kcal/mole above the folded ensemble and exhibit a molar volume that is ~20 ml/mol smaller than the native tRNA. This value is about half that observed for G-quadruplex disruption (40, 56). While double-stranded DNA and DNA hairpins exhibit both positive and negative volume changes for melting (~-5 to +5 ml/mol base pair), depending upon sequence and conditions (64–66), volume changes for the pressure-induced disruption of RNA tetra-loops or ribozymes were found to be ~-7 and -25 ml/mol, respectively (38, 43, 44). Pressure-induced disruption of nucleic acids, including RNA structures, is due to increased hydration, electrostriction of ions and loss of cavities in the disrupted states (56, 67). The value reported here for the pressure-induced conformational change of unmodified $tRNA^{Lys3}$ (~-20 ml/mol) is equivalent to the molar volume of a water molecule and could correspond to local penetration of the structure by water.

While the pressure-induced changes observed here in the imino proton ^{1}H-^{15}N HSQC spectrum of unmodified $tRNA^{Lys3}$ were very large, the SAXS profiles showed changes in shape, but not size (R_g) at HP. However, the small change in R_g was accompanied by a significant change in shape. In SAXS experiments on yeast $tRNA^{Phe}$, Fang and coworkers (68) reported a very small (< 1 Å) increase in R_g upon decreasing Mg^{2+} concentration from 1 mM to 0.1 mM, similar to the small increase observed here with $tRNA^{Lys3}$ at HP. Molecular dynamics simulations and ensemble optimization of our HP-SAXS results produced conformational ensembles that describe very well the SAXS profiles at low and high pressure. The optimized configurations of the HP-SAXS profile reveal disruption and distortion of structure in the region adjoining the T-loop, the stacking of the Acceptor and T-stems, the D-stem and the top of the anti-codon stem, as well as relative reorientations of the anticodon, T and D loops. These disrupted structures are consistent with the NMR detected decrease in base pair stability in the acceptor stem (G5, G6, G69, G70 and U 67), the T-loop (U 54, U55 and U64), the stacking between these two structures, the D stem/loop (U8, U12, G15 and G24) and the top of the anti-codon stem (G30, U41 and G42) at high pressure. Even when base pairs remain in the EOM selected structures, the pressure-induced distortions (bends, widening of helices, etc) that are apparent in the SAXS profiles as a change in shape of the molecule, can lead to significant destabilization of the base pairs, such that their solvent exchange becomes fast on the NMR timescale, and imino proton intensity is lost. SAXS data represent an equilibrium ensemble, whereas the NMR peak intensities are affected by the timescales of the dynamics.

One of us has previously determined the secondary structure of the $tRNA^{Lys3}$/HIV RNA complex (49) (Figure 6). In this complex, 18 bases in the 3'-end of $tRNA^{Lys3}$, including most of the acceptor stem, hybridize with bases from the HIV RNA to form a long, stable double helix, while bases from the tRNA T-loop form a new intramolecular helix with bases at the 5'-end of the acceptor stem. The D-stem/loop and the anti-codon stem/loop regions retain their original secondary structure in the complex, but chemical shift perturbations suggested that their tertiary interactions are modified. The significant disruption observed here of the acceptor stem, and towards the T-loop in the optimized ensemble structures at 3000 bar suggest that these excited states of $tRNA^{Lys3}$ could be exploited by the HIV RNA in the hijacking of the tRNA (69) for reverse transcription of the viral RNA. Note that the tRNA used in the present study was unmodified, while that hijacked *in vivo* by the HIV virus presents all of the known stabilizing post-transcriptional modifications. Thus, *in vivo*, any excited states exploited by the virus would lie at

higher free energies, relative to the native state of the tRNA. Nonetheless, such states could still play an important role in the interaction with the viral RNA. Overall these studies demonstrate the utility of HP in combination with 2D-NMR, SAXS and computation to quantify the local stability of RNA, to favor the population of excited RNA conformational states and to characterize their structure and energetics. The high pressure NMR system used in these studies (70) is straightforward to implement. A wide variety of multi-dimensional NMR methods have been coupled to high pressure in the study of protein conformation and dynamics, including high pressure DOSY (71), RDC (72), ZZ-exchange (73), and relaxation approaches such as T1/T2/NOE (74), CPMG (75), and CEST (76). Combining such approaches with pressure should likewise prove insightful in the study of RNA conformational landscapes. For example, using higher fields than were available in the present work, more in-depth structural information about high pressure states of RNA could be derived from constraints obtained from a combination of SAXS and RDC measurements as has been done at atmospheric pressure previously (*e.g.,* (77)). Likewise, further investigation of hydrogen bonding properties at high pressure of larger RNA molecules, such as the $tRNA^{Lys3}$ studied here, could make use of optimized HNN-COSY experiments (79, 80).

Materials and Methods

Purification of T7 RNA polymerase

The plasmid harboring the T7 RNA polymerase gene from the Puglisi lab was transformed into E. coli BL21 (DE3) competent cells (NEB). The cells containing the T7 RNA polymerase construct were grown in LB media containing ampicillin (final working concentration of 100 µg/mL), induced with a 500 µM IPTG final concentration and shaken at 220 rpm for 18 hours at 19°C. The cells were harvested, the pellets were re-suspended in lysis buffer and lysis was performed using sonication. The lysate was centrifuged, the supernatant was loaded on Ni-NTA beads, and the protein was eluted with 100 mM imidazole. Care was taken to use nuclease free water for all buffers used in the purification. PMSF was used as a protease inhibitor.

In vitro Transcription of $tRNA^{Lys3}$

The purified RNA polymerase was used for in vitro transcription of $tRNA^{Lys3}$ as described elsewhere (81). Briefly, to a mixture containing 50mM NTPs, DNA template, 22mM MgCl2 and 1M DTT, the in-house purified T7 polymerase was added and incubated at 37°C for 6 hours. The transcription reaction was stopped by adding 0.5 M EDTA. The tRNA obtained was purified in a two-step process. The first step involves removal of T7 polymerase and template DNA from the mixture using phenol/chloroform precipitation. The entire RNA from the aqueous layer of the phenol/chloroform extraction step was subjected to electrophoresis followed by electro-elution to obtain pure RNA. For NMR the RNA molecule was selectively labeled by incorporating ^{15}N-GTP and 15N-UTP into the NTP mix of the in vitro transcription.

High-pressure NMR

NMR peak assignments of $tRNA^{Lys3}$ were obtained from Puglisi et. al (51). NMR experiments were performed on a Bruker Avance III 600 MHz spectrometer (Bruker, Billerica, MA) at the NMR Core Facility, Center for Biotechnology and Interdisciplinary Studies, RPI. For the high-pressure experiments a special 5-mm pressure-resistant zirconium tube was used, and hydrostatic pressure was applied on the sample using the Xtreme Syringe pump (Daedalus Innovations, Aston, PA). The sample solution contained 0.75mM $tRNA^{Lys3}$ at pH 6.5 and 0.4 mM at pH 5.5 in 100 mM NaCl, 10% D_2O, 10 mM MES buffer (pH 6.5 or 5.5) and 1-20 mM $MgCl_2$. At each Mg^{2+} concentration (1mM, 10mM and 20mM) a series of 1D ^{1}H and 2D [^{1}H-^{15}N] HSQC spectra were recorded at equilibrium as a function of pressure, in the range of 1-3000 bar and at 25°C. A 1D ^{1H} jump-return and 2D ^{1}H-^{15}N HSQC pulse sequence utilizing selective water flip-back pulses were employed to minimize water saturation (82). The pressure increments were in steps

of 200 bar. After each pressure increment, an equilibration time of 10 minutes was allowed for the RNA molecule to reach its steady state and the spectral acquisition was performed. All 2D spectra were recorded with 16 time averaged scans, with an inter-scan delay of 2 seconds, and spectral widths of 24.49 and 26.00 ppm with 4096 and 160 points acquired in ^{1}H and ^{15}N dimensions respectively.

NMR Data Analysis

From each HSQC spectra, the folded state intensities for each imino group were fit separately using nonlinear least-square method to a two-state model (U ⇌ F) as a function of pressure *(p)*,

$$I(p) = (I_u + I_f e^{((\Delta Go - p\Delta Vf)/RT)})/(1+e^{((\Delta Go - p\Delta Vf)/RT)}) \quad (1)$$

The resulting fit provides nucleotide-specific apparent change in free energy at ambient pressure (ΔG_f) and apparent change in volume upon folding (ΔV_f). The data fitting was performed in Bioeqs program (83) or a MatLab script. The high pressure plateau value was fixed at 0 for all profiles, since the folded state intensity should disappear completely in the final state. The low pressure plateau values for fitting data from 1 and 10 mM concentrations were fixed to a value at ~10% higher than the intensity at 10 bar.

High-Pressure SAXS

High-Pressure SAXS was performed at the ID7A beamline station that is a part of the Cornell High Energy Synchrotron Source (CHESS) (84) as described previously (85). All the experiments were performed in the pressure range of 1-3000 bar and the pressure was maintained by a Barocycler HUB440 high pressure pump (Pressure BioSciences). The frozen samples were equilibrated on ice, followed by equilibration at room temperature. The samples were finally centrifuged at 14,000 rpm for 30 minutes before loading into the new plastic sample cell as described (86). HPSAXS was performed on $tRNA^{Lys3}$ with 20 exposures of 0.5 seconds each. The sample solution used for SAXS acquisition was 10 mg/ml $tRNA^{Lys3}$ in 10mM MES buffer (pH 6.5), 100 mM NaCl, and 1-20 mM $MgCl_2$ concentration as described above. The 2D SAXS profiles were then integrated about the beam center and buffer subtracted using BioXTAS RAW 2.0.1 package (87). The radius of gyration was calculated using Guinier analysis, the Kratky plots and normalized Kratky plots were generated in BioXTAS RAW 2.0.1 package. The pair distance distribution function (P(r)) was calculated using GNOM package (88)) of ATSAS suite (89, 90) integrated into the RAW package.

Temperature dependent structure based modeling

All-atom structure based potentials were generated from the PDB entry 1FIR using SMOG (version 2.0.3) web server http://smog-server.org (46) with default parameter sets (91). The contacts were identified from PDB coordinates through use of the Shadow Contact Map algorithm (92) with a cutoff distance of 6 Å, shadowing radius of 1 Å and residue sequence separations of 3. Atom pairs that are not identified as contacts are assigned an excluded volume interaction. The bond lengths and angles, improper and planar dihedral angles of the protein are maintained by harmonic potentials. The potentials are assigned such that the native configuration of each bond and angle is considered the minimum. The final form of the potential energy function for AA-SBM model is:

$$V = \sum_{bonds} \varepsilon_r (r - r_o)^2 + \sum_{angles} \varepsilon_\Theta (\Theta - \Theta_o)^2 + \sum_{\substack{improper \\ /planar}} \varepsilon_\chi (\chi - \chi_o)^2 + \sum_{backbone} \varepsilon_{BB} F_D(\phi)$$
$$+ \sum_{side-chain} \varepsilon_{SC} F_D(\phi) + \sum_{contact} \left\{ \varepsilon_C(i,j) \left[a \left(\frac{\sigma_{ij}}{r_{ij}} \right)^{12} - b \left(\frac{\sigma_{ij}}{r_{ij}} \right)^{6} \right] \right\}$$
$$+ \sum_{non-contact} \varepsilon_{NC}(i,j) \left(\frac{\sigma_{ij}}{r_{ij}} \right)^{12}$$

$$F_D(\phi) = [1 - \cos(\phi - \phi_o)] + \left[1 - \cos\left(3(\phi - \phi_o)\right)\right]/2$$

with all parameters having the default values as reported in (91).

Gromacs 4.6.7 was used as the computation engine to run the simulations (93). To enhance sampling efficiency and accelerate equilibration, the replica exchange molecular dynamics (REMD) method (94) as implemented in Gromacs (93) was employed. We used 24 replicas from 94 to 116K spaced by 1 K. Exchange was attempted every 5000 time steps, and coordinates were saved every 1000 integration steps. REMD was combined with Langevin dynamics (time step τ = 0.0005 ps) for $5 \cdot 10^8$ time steps per replica. The fraction of native contacts (defined as any native pair within 1.5 times the native distance) formed as a function of time, Q, was used as a global reaction coordinate.

EOM based Modelling and DENSS ab initio electron Density Maps

Ensemble optimization method (EOM) was performed using GAJOE (Genetic Algorithm Judging Optimization of Ensemble) (47, 58) in the ATSAS suite. The starting structures for the modelling were obtained from MD simulations. The complete ensemble obtained from the MD simulations (58) were selected according to their percentage of native contacts (Q) with each representative cluster containing 10,000 structures spanning a Q range of 0.02 (overall Q range used was 0.84-1.0). Using GAJOE, subsets of theoretical SAXS profiles calculated from the ensemble were compared to the experimental SAXS profiles and those structures which fit to the experimental SAXS profiles with minimal $\chi 2$ values were chosen as representatives of the SAXS profiles. A total of 5000 generations were employed in the genetic algorithm. A total of 200 cycles of independent genetic algorithm runs were performed. *Ab initio* electron density calculations were performed using DENSS (95) and the input for the calculations was the P(r) data obtained from GNOM. For each conformation 20 reconstructions were performed in slow mode with all other parameters set to default.

Acknowledgments

This work was partially supported by NSF CLP 1610691 to CAR and NIH grant AI150464 to EVP and NSF CLP-1803045 to GIM. We also thank Pau Bernadó and Amin Sagar for assistance in using EOM.

References

1. Al-Hashimi HM, Walter NG (2008) RNA dynamics: it is about time. *Curr Opin Struct Biol* 18(3):321–329.
2. Dethoff EA, Chugh J, Mustoe AM, Al-Hashimi HM (2012) Functional complexity and regulation through RNA dynamics. *Nature* 482(7385):322–330.
3. Dethoff EA, Petzold K, Chugh J, Casiano-Negroni A, Al-Hashimi HM (2012) Visualizing transient low-populated structures of RNA. *Nature* 491(7426):724–728.
4. Yang Y, et al. (2022) Structural basis of RNA conformational switching in the transcriptional regulator 7SK RNP. *Mol Cell*:1724–1736.
5. Sutton JL, Pollack L (2015) Tuning RNA Flexibility with Helix Length and Junction Sequence. *Biophys J* 109(12):2644–2653.
6. Haller A, Soulière MF, Micura R (2011) The dynamic nature of RNA as key to understanding riboswitch mechanisms. *Acc Chem Res* 44(12):1339–1348.
7. Hall KB (2013) RNA does the folding dance of twist, turn, stack. *Proc Natl Acad Sci U S A* 110(42):16706–7.
8. Welty R, et al. (2018) Divalent ions tune the kinetics of a bacterial GTPase center rRNA folding transition from secondary to tertiary structure. *RNA* 24(12):1828–1838.
9. Ganser LR, Kelly ML, Herschlag D, Al-Hashimi HM (2020) The roles of structural dynamics in the cellular functions of RNAs. *Nat Rev Mol Cell Biol* 20(8):474–489.
10. Mustoe AM, et al. (2015) Noncanonical Secondary Structure Stabilizes Mitochondrial tRNA $^{Ser(UCN)}$ by Reducing the Entropic Cost of Tertiary Folding. *J Am Chem Soc* 137(10):3592–3599.
11. Li Q, et al. (2009) Germline mutation of microRNA-125a is associated with breast cancer. *J Med Genet* 46:358–360.
12. Dallaire P, et al. (2016) Structural dynamics control the MicroRNA maturation pathway. *Nucleic Acids Res* 44(20):9956–9964.
13. Kutchko KM, et al. (2015) Multiple conformations are a conserved and regulatory feature of the RB1 5' UTR. *RNA* 21(7):1274–1285.
14. Halvorsen M, Martin JS, Broadaway S, Laederach A (2010) Disease-associated mutations that alter the RNA structural ensemble. *PLoS Genet* 6(8):1–11.
15. Mustoe AM, Brooks CL, Al-Hashimi HM (2014) Topological constraints are major determinants of tRNA tertiary structure and dynamics and provide basis for tertiary folding cooperativity. *Nucleic Acids Res* 42(18):11792–11804.
16. Pütz J, Puglisi JD, Florentz C, Giegé R (1991) Identity elements for specific aminoacylation of yeast tRNA(Asp) by cognate aspartyl-tRNA synthetase. *Science (80-)* 252(5013):1696–9.
17. Lee T-H, Blanchard SC, Kim HD, Puglisi JD, Chu S (2007) The role of fluctuations in tRNA selection by the ribosome. *Proc Natl Acad Sci U S A* 104(34):13661–5.
18. Kleiman L (2002) tRNALys3: The primer tRNA for reverse transcription in HIV-1. *IUBMB Life* 53(2):107–114.
19. Latham MP, Brown DJ, McCallum SA, Pardi A (2005) NMR methods for studying the structure and dynamics of RNA. *ChemBioChem* 6(9):1492–1505.
20. Hengesbach M, Kim NK, Feigon J, Stone MD (2012) Single-molecule FRET reveals the folding dynamics of the human telomerase rna pseudoknot domain. *Angew Chemie - Int Ed* 51(24):5876–5879.
21. Kobitski AY, et al. (2011) Single-molecule FRET reveals a cooperative effect of two methyl group modifications in the folding of human mitochondrial tRNA(Lys). *Chem Biol* 18(7):928–36.
22. Bisaria N, Herschlag D (2015) Probing the kinetic and thermodynamic consequences of the tetraloop / tetraloop receptor monovalent ion-binding site in P4 – P6 RNA by smFRET. *Biochem Soc Trans* 43:172–178.

23. Bai Y, et al. (2007) Quantitative and comprehensive decomposition of the ion atmosphere around nucleic acids. *J Am Chem Soc* 129(48):14981–14988.
24. Solomatin S V, Greenfeld M, Chu S, Herschlag D (2010) Multiple native states reveal persistent ruggedness of an RNA folding landscape. *Nature* 463(7281):681–684.
25. Feng XA, Poyton MF, Ha T (2021) Multicolor single-molecule FRET for DNA and RNA processes. *Curr Opin Struct Biol* 70:26–33.
26. Hall KB (2009) 2-aminopurine as a probe of RNA conformational transitions. *Methods Enzymol* 469(09):269–285.
27. Pollack L (2011) Time resolved SAXS and RNA folding. *Biopolymers* 95(8):543–549.
28. Shi X, Walker P, Harbury PB, Herschlag D (2017) Determination of the conformational ensemble of the TAR RNA by X-ray scattering interferometry. *Nucleic Acids Res* 45(8):1–10.
29. Garcia AE, Paschek D (2008) Simulation of the pressure and temperature folding/unfolding equilibrium of a small RNA hairpin. *J Am Chem Soc* 130(3):815–7.
30. Nguyen HT, Hori N, Thirumalai D (2019) Theory and simulations for RNA folding in mixtures of monovalent and divalent cations. *Proc Natl Acad Sci U S A* 116(42):21022–21030.
31. Hayes RL, et al. (2012) Magnesium fluctuations modulate RNA dynamics in the SAM-I riboswitch. *J Am Chem Soc* 134(29):12043–12053.
32. Chen YL, Sutton JL, Pollack L (2018) How the Conformations of an Internal Junction Contribute to Fold an RNA Domain. *J Phys Chem B* 122(49):11363–11372.
33. Xue Y, et al. (2015) Characterizing RNA excited states using NMR relaxation dispersion. *Methods in Enzymology* (Elsevier Inc.), pp 39–73. 1st Ed.
34. Heremans K, Smeller L (1998) Protein structure and dynamics at high pressure. *Biochim Biophys Acta* 1386(2):353–370.
35. Silva JL, Foguel D, Royer CA (2001) Pressure provides new insights into protein folding, dynamics and structure. *Trends Biochem Sci* 26(10):612–8.
36. Tobé S, et al. (2005) The catalytic mechanism of hairpin ribozyme studied by hydrostatic pressure. *Nucleic Acids Res* 33(8):2557–2564.
37. Hervé G, Tobé S, Heams T, Vergne J, Maurel M-C (2006) Hydrostatic and osmotic pressure study of the hairpin ribozyme. *Biochim Biophys Acta - Proteins Proteomics* 1764(3):573–577.
38. Downey CD, Crisman RL, Randolph TW, Pardi A (2007) Influence of hydrostatic pressure and cosolutes on RNA tertiary structure. *J Am Chem Soc* 129(30):9290+.
39. Gao M, Arns L, Winter R (2017) Modulation of the Thermodynamic Signatures of an RNA Thermometer by Osmolytes and Salts. *Angew CHEMIE-INTERNATIONAL Ed* 56(9):2302–2306.
40. Harish B, et al. (2022) Hidden intermediates in Mango III RNA aptamer folding revealed by pressure perturbation. *Biophys J* 121(3):421–429.
41. Schuabb C, Berghaus M, Rosin C, Winter R (2015) Exploring the Free Energy and Conformational Landscape of tRNA at High Temperature and Pressure. *ChemPhysChem* 16(1):138–146.
42. Fedoruk-Wyszomirska A, Wyszko E, Giel-Pietraszuk MM, Barciszewska MZMZ, Barciszewski J (2007) High hydrostatic pressure approach proves RNA catalytic activity without magnesium. *Int J Biol Macromol* 41(1):30–35.
43. Giel-Pietraszuk M, Fedoruk-Wyszomirska A, Barciszewski J (2010) Effect of high hydrostatic pressure on hydration and activity of ribozymes. *Mol Biol Rep* 37(8):3713–3719.
44. Giel-Pietraszuk MM, Barciszewski J (2012) Hydrostatic and osmotic pressure study of the RNA hydration. *Mol Biol Rep* 39(5):6309–6318.
45. Giel-Pietraszuk M, Barciszewski J (2005) A nature of conformational changes of yeast

tRNAPhe. *Int J Biol Macromol* 37(3):109–114.
46. Noel JK, et al. (2016) SMOG 2: A Versatile Software Package for Generating Structure-Based Models. *PLoS Comput Biol* 12(3):1–14.
47. Tria G, Mertens HDT, Kachala M, Svergun DI (2015) Advanced ensemble modelling of flexible macromolecules using X-ray solution scattering. *IUCrJ* 2:207–217.
48. Bénas P, et al. (2000) The crystal structure of HIV reverse-transcription primer tRNA(Lys,3) shows a canonical anticodon loop. *RNA* 6(10):1347–1355.
49. Puglisi EV, Puglisi JD (2011) Secondary Structure of the HIV Reverse Transcription Initiation Complex by NMR. *J Mol Biol* 410(5):863–874.
50. Lukavsky PJ, Puglisi JD (2004) Large-scale preparation and purification of polyacrylamide-free RNA oligonucleotides. *RNA* 10(5):889–93.
51. Puglisi EV, Puglisi JD (2007) Probing the conformation of human tRNA Lys in solution by NMR. 581:5307–5314.
52. Vermeulen A, McCallum SA, Pardi A (2005) Comparison of the global structure and dynamics of native and unmodified tRNAval. *Biochemistry* 44:6024–6033.
53. Snoussi K, Leroy JL (2001) Imino proton exchange and base-pair kinetics in RNA duplexes. *Biochemistry* 40(30):8898–8904.
54. Guéron M, Kochoyan M, Leroy JL (1988) A single mode of DNA base-pair opening drives imino proton exchange. *Nature* 328(6125):89–92.
55. Quinlan RJ, Reinhart GD (2005) Baroresistant buffer mixtures for biochemical analyses. *Anal Biochem* 341(1):69–76.
56. Fan HY, et al. (2011) Volumetric characterization of sodium-induced G-quadruplex formation. *J Am Chem Soc* 133(12):4518–4526.
57. Ozenne V, et al. (2012) Flexible-meccano: a tool for the generation of explicit ensemble descriptions of intrinsically disordered proteins and their associated experimental observables. *Bioinformatics* 28(11):1463–70.
58. Bernadó P, Mylonas E, Petoukhov M, Blackledge M, Svergun DI (2007) Structural characterization of flexible proteins using small-angle X-ray scattering. *J Am Chem Soc* 129(17):5656–5664.
59. Bernadó P, Blackledge M (2009) A self-consistent description of the conformational behavior of chemically denatured proteins from NMR and small angle scattering. *Biophys J* 97(10):2839–45.
60. Sagar A, Jeffries C, Petoukhov M, Svergun D, Bernad P (2021) Comment on the Optimal Parameters to Derive Intrinsically Disordered Protein Conformational Ensembles from Small-Angle X-ray Scattering Data Using the Ensemble Optimization Method. *J Chem Theory Comput* 17:2014–2021.
61. Cheng P, Peng J, Zhang Z (2017) SAXS-Oriented Ensemble Refinement of Flexible Biomolecules. *Biophys J* 112(7):1295–1301.
62. Dagenais P, Desjardins G, Legault P (2021) An integrative NMR-SAXS approach for structural determination of large RNAs defines the substrate-free state of a trans-cleaving Neurospora Varkud Satellite ribozyme. *Nucleic Acids Res* 49(20):11959–11973.
63. Whitford PC, et al. (2009) Nonlocal helix formation is key to understanding s-adenosylmethionine-1 riboswitch function. *Biophys J* 96(2):L7–L9.
64. Amiri AR, Macgregor RB (2011) The effect of hydrostatic pressure on the thermal stability of DNA hairpins. *Biophys Chem* 156(1):88–95.
65. Rayan G, Macgregor Jr. RB (2015) A look at the effect of sequence complexity on pressure destabilisation of DNA polymers. *Biophys Chem* 199:34–38.
66. Makhatadze GI, Chen CR, Khutsishvili I, Marky LA (2022) The volume changes of unfolding of dsDNA. *Biophysj* c:1–8.
67. Rayan G, Macgregor R (2009) Pressure-induced helix-coil transition of DNA copolymers is linked to water activity. *Biophys Chem* 144(1–2):62–66.

68. Fang X, et al. (2000) Mg2+-dependent compaction and folding of yeast tRNAPhe and the catalytic domain of the B. subtilis RNase P RNA determined by small-angle X-ray scattering. *Biochemistry* 39(36):11107–11113.
69. Larsen K, et al. (2018) Architecture of an HIV-1 reverse transcriptase initiation complex. *Nature* 557:118–122.
70. Peterson RW, Wand AJ (2005) Self-contained high-pressure cell, apparatus, and procedure for the preparation of encapsulated proteins dissolved in low viscosity fluids for nuclear magnetic resonance spectroscopy. *Rev Sci Instrum* 76(9):094101.
71. Gao M, et al. (2017) Temperature and pressure limits of guanosine monophosphate self-assemblies. *Sci Rep* 7(1):9864.
72. Fu Y, Wand AJ (2013) Partial alignment and measurement of residual dipolar couplings of proteins under high hydrostatic pressure. *J Biomol NMR* 56(4):353–357.
73. Zhang Y, et al. (2016) High Pressure ZZ-Exchange NMR Reveals Key Features of Protein Folding Transition States. *J Am Chem Soc* 138(46):15260–15266.
74. Fu Y, et al. (2012) Coupled Motion in Proteins Revealed by Pressure Perturbation. *J Am Chem Soc* 134(20):8543–8550.
75. Korzhnev DM, et al. (2006) Probing the transition state ensemble of a protein folding reaction by pressure-dependent NMR relaxation dispersion. *J Am Chem Soc* 128(15):5262–9.
76. Zhang S, McCallum SA, Gillilan RE, J. W, Royer CA (2022) High Pressure CPMG and CEST Reveal that Cavity Position Dictates Distinct Dynamic Disorder in the PP32 Repeat Protein. *J Phys Chem B*.
77. Grishaev A, Ying J, Canny MD, Pardi A, Bax A (2008) Solution structure of tRNAVal from refinement of homology model against residual dipolar coupling and SAXS data. *J Biomol NMR* 42(2):99–109.
78. Sibille N, Dellarole M, Royer C, Roumestand C (2014) Measuring residual dipolar couplings at high hydrostatic pressure: robustness of alignment media to high pressure. *J Biomol NMR* 58(1):9–16.
79. Dallmann A, et al. (2013) Efficient detection of hydrogen bonds in dynamic regions of RNA by sensitivity-optimized NMR pulse sequences. *Angew Chemie - Int Ed* 52(40):10487–10490.
80. Farjon J, et al. (2009) Longitudinal-relaxation-enhanced NMR experiments for the study of nucleic acids in solution. *J Am Chem Soc* 131(24):8571–8577.
81. Puglisi JD, Wyatt JR (1995) Biochemical and NMR studies of RNA conformation with an emphasis on RNA pseudoknots. *Methods Enzymol* 261(C):323–350.
82. Grzesiek S, Bax A (1993) The importance of not saturatin H2O in protein NMR. (12):12593–12594.
83. Royer CA, Beechem JM (1992) *Numerical analysis of binding data: Advantages, practical aspects, and implications* doi:10.1016/0076-6879(92)10025-9.
84. Ando N, Chenevier P, Novak M, Tate MW, Gruner SM (2008) High hydrostatic pressure small-angle X-ray scattering cell for protein solution studies featuring diamond windows and disposable sample cells. *J Appl Crystallogr* 41(1):167–175.
85. Jenkins KA, et al. (2018) The consequences of cavity creation on the folding landscape of a repeat protein depend upon context. *Proc Natl Acad Sci* 115(35):E8153–E8161.
86. Rai DK, et al. (2021) High-pressure small-angle X-ray scattering cell for biological solutions and soft materials. *J Appl Crystallogr* 54(1):111–122.
87. Hopkins JJB, Gillilan RRE, Skou S (2017) BioXTAS RAW: Improvements to a Free Open-Source Program for Small-Angle X-Ray Scattering Data Reduction and Analysis. *J Appl Crystallogr* 50(5):1545–1553.
88. Semenyuk AV, Svergun DI (1991) GNOM. A program package for small-angle scattering data processing. *J Appl Crystallogr* 24(pt 5):537–540.

89. Petoukhov M, et al. (2012) New developments in the ATSAS program package for small-angle scattering data analysis. *J Appl Crystallogr* 45(2):342–350.
90. Manalastas-Cantos K, et al. (2021) ATSAS 3.0: Expanded functionality and new tools for small-angle scattering data analysis. *J Appl Crystallogr* 54:343–355.
91. Whitford PC, et al. (2009) An all-atom structure-based potential for proteins: Bridging minimal models with all-atom empirical forcefields. *Proteins Struct Funct Bioinforma* 75(2):430–441.
92. Noel JK, Whitford PC, Onuchic JN (2012) The shadow map: a general contact definition for capturing the dynamics of biomolecular folding and function. *J Phys Chem B* 116(29):8692–8702.
93. Hess B, Kutzner C, Van Der Spoel D, Lindahl E (2008) GROMACS 4: Algorithms for highly efficient, load-balanced, and scalable molecular simulation. *J Chem Theory Comput* 4(3):435–447.
94. Sugita Y, Okamoto Y (1999) Replica exchange molecular dynamics method for protein folding simulation. *Chem Phys Lett* 314:141–151.
95. Grant TD (2018) Ab initio electron density determination directly from solution scattering data. *Nat Methods* 15(3):191–193.

Figure Legends

Figure 1. Effects of pressure on the imino proton spectrum of unmodified $tRNA^{Lys3}$. A, B) Structure of $tRNA^{Lys3}$ reproduced from the structure of native $tRNA^{Lys3}$ (including all natural base modifications), pdb code:1fir (48). In A) are highlighted the base pair partners (green) of the bases (red) for which imino proton peaks are imino proton resonances are assigned (51) and detected. In B0 are highlighted the bases for which imino proton peaks could be quantified as a function of pressure. The acceptor stem is colored in red, the T-loop in pink, the D-stem/loop in blue and the anti-codon stem/loop in green. Bases for which and quantified in the present study are shown in filled rings. The bases for which pressure-dependent imino proton intensities were quantified are labeled. C-F) Pressure effects on $tRNA^{Lys3}$ imino proton ^{1}H-^{15}N HSQC spectrum; C) and D) guanosine nucleotides, E) and F) uridine nucleotides at C) and D) 1 mM $MgCl_2$, E) and F) 20 mM $MgCl_2$. G) Pressure dependence of the imino proton peak intensities for $tRNA^{Lys3}$ at 1 mM MgCl2. Data are plotted as normalized intensity profiles. Data were ft and then both data and fit were normalized. G5 – open red circles, G6 – red squares, U8 – beige circles, G10 - beige triangles, U12 - blue circles, G24 – blue squares, U41 - green circles, G42 – green open circles, G52 – pink squares, U54 – pink circles, U64 – open pink circles, U67 – red circles, U70 – red triangles. Colors of data points and fitted lines represent the structural regions of the tRNA as depicted in B.

Figure 2. Effect of MgCl2 concentration on the NMR-detected pressure-induced transition of $tRNA^{Lys3}$. A-D) Four bases, G5, G42, G52 and U64 that showed very little change in peak intensity at 20 mM $MgCl_2$. E-F) Two bases, U8 and U12, that showed significant loss in intensity at 20 mM $MgCl_2$. Red – 1 mM $MgCl_2$, blue – 10 mM $MgCl_2$, green 20 mM $MgCl_2$. G) Cartoon representation of the structure of $tRNA^{Lys3}$ (pdb:1fir)(48) with the crystallographically determined Mg^{2+} and Na^{+} ions in pink and purple spheres, respectively. The four bases G5, G42, G52 and U64, that exhibit strong stabilization at 20 mM $MgCl_2$ are shown in stick representation and are labeled.

Figure 3. HP SAXS results for $tRNA^{Lys3}$. A) SAXS intensity profiles, B) Pair distance distribution (P(r)) plots, C) Normalized Kratky plots and D) Pressure dependence of the radius of gyration (R_g) calculated from the P(r) profiles. Blue – 10 bar; red 3000 bar.

Figure 4. Ensemble Optimization of tRNALys3 at 10 bar. A) SAXS intensity profile and B) P(r) distribution with experimental results (open blue circles) with the fit from EOM (black (A) or blue (B) line) optimization resulting in the three configurations in C-E). C-E) The three models that best describe the SAXS profiles recovered from EOM as described in the Methods section labeled for the configuration number and relative population in the final fitted ensemble. For each configuration the cartoon structure with orange backbone and green filled bases (left) and the electron density (right) calculated using Chimera (ref). Red is highest density, blue is lowest. The structure on the left is fitted in the electron density using Chimera.

Figure 5. Ensemble Optimization of tRNALys3 at 3000 bar. A) SAXS intensity profile and B) P(r) distribution with experimental results (open red circles) with the fit from EOM (black or red line) with the five configurations in C-G). C-F) The five models that best describe the SAXS profiles recovered from EOM as described in the Methods section labeled for the configuration number and relative population in the final fitted ensemble. For each configuration the cartoon structure with orange backbone and green filled bases (left) and the electron density (right) calculated using Chimera (95). Red is highest density, blue is lowest. The structure on the left is fitted in the electron density using Chimera.

Figure 6. Secondary structure of the tRNALys3-HIV initiation complex. The secondary structure represented in this figure was previously determined by NMR (49) and is reproduced here.

Figures

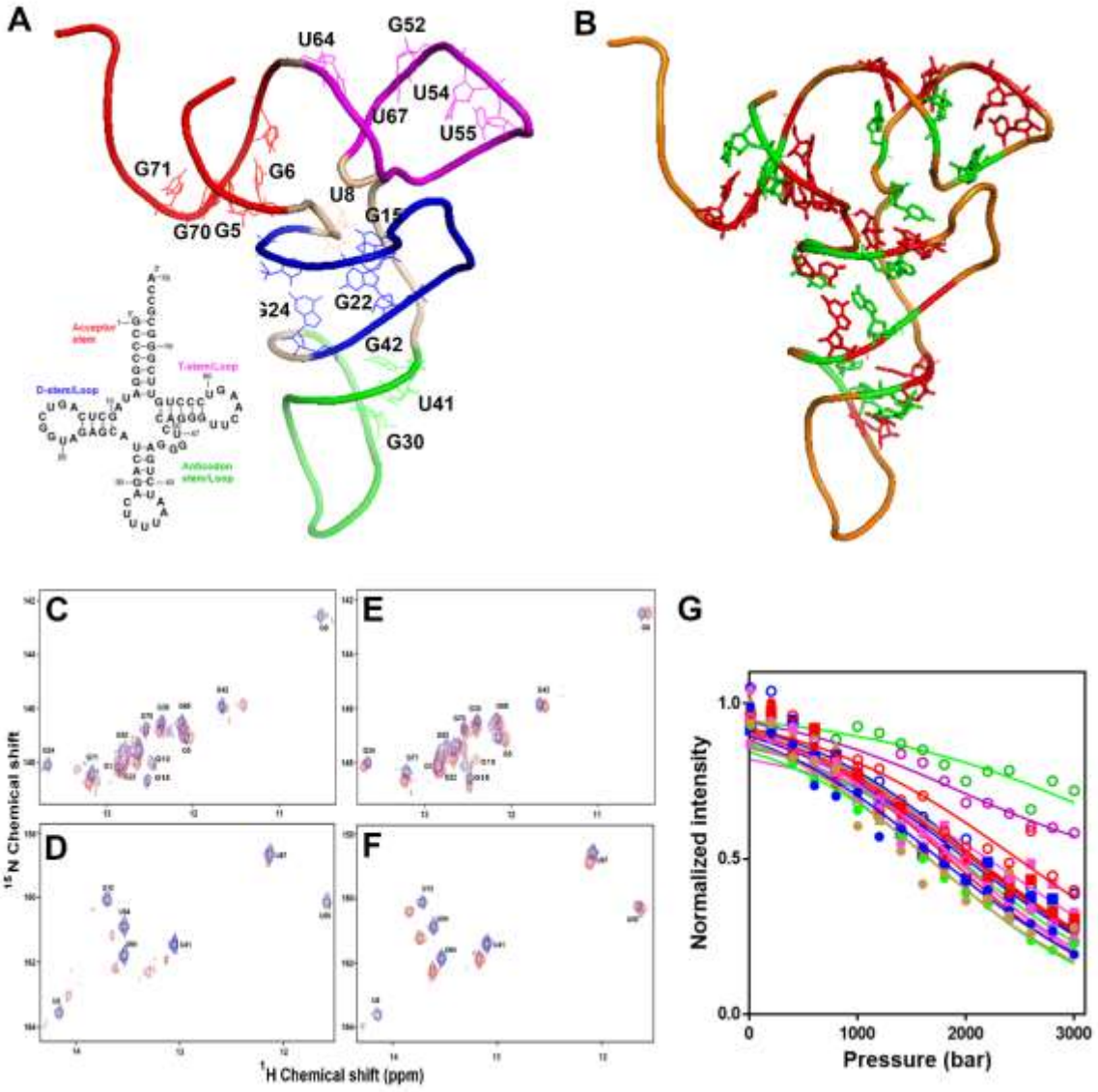

Figure 1. Effects of pressure on the imino proton spectrum of unmodified tRNA^{Lys3}. A, B) Structure of tRNA^{Lys3} reproduced from the structure of native tRNA^{Lys3} (including all natural base modifications), pdb code:1fir (48). In A are highlighted the bases for which imino proton peaks were detected are shown in stick and are labeled. The acceptor stem is colored in red, the T-loop in pink, the D-stem/loop in blue and the anti-codon stem/loop in green. The secondary structure is shown in the inset. In B) are highlighted the base pair partners (green) of the bases (red) for which imino proton peaks are assigned (51) and detected. C-F) Pressure effects on tRNA^{Lys3} imino proton ^{1}H-^{15}N HSQC spectrum; C) and D) guanosine nucleotides, E) and F) uridine nucleotides at C) and D) 1 mM $MgCl_2$, E) and F) 20 mM $MgCl_2$. Spectra are overlaid for 1 bar (blue) and 3000 bar (red). G) Pressure dependence of the imino proton peak intensities for tRNA^{Lys3} at 1 mM MgCl2. Data are plotted as normalized intensity profiles. Data were fit and then both data and fit were normalized. G5 – open red circles, G6 – red squares, U8 – beige circles, U12 - blue circles, G15, beige triangles, G24 – blue squares, G30 – open purple circles, U41 - green circles, G42 – green open circles, G52 – pink squares, U54 – pink circles, U55 – open blue circles, U64 – open pink circles, U67 – red circles, G69 – open green circles, G70 – red triangles.

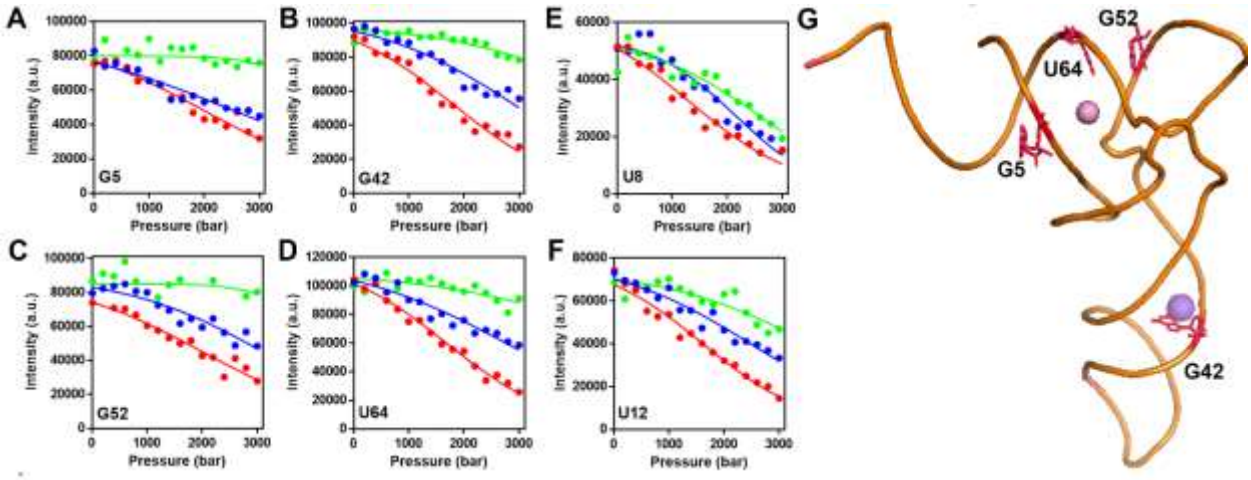

Figure 2. Effect of MgCl2 concentration on the NMR-detected pressure-induced transition of $tRNA^{Lys3}$. A-D) Four bases, G5, G42, G52 and U64 that showed very little change in peak intensity at 20 mM $MgCl_2$. E-F) Two bases, U8 and U12, that showed significant loss in intensity at 20 mM $MgCl_2$. Red – 1 mM $MgCl_2$, blue – 10 mM $MgCl_2$, green 20 mM $MgCl_2$. G) Cartoon representation of the structure of $tRNA^{Lys3}$ (pdb:1fir)(48) with the crystallographically determined Mg^{2+} and Na^{+} ions in pink and purple spheres, respectively. The four bases G5, U42, G52 and U64, that exhibit strong stabilization at 20 mM $MgCl_2$ are shown in stick representation and are labeled.

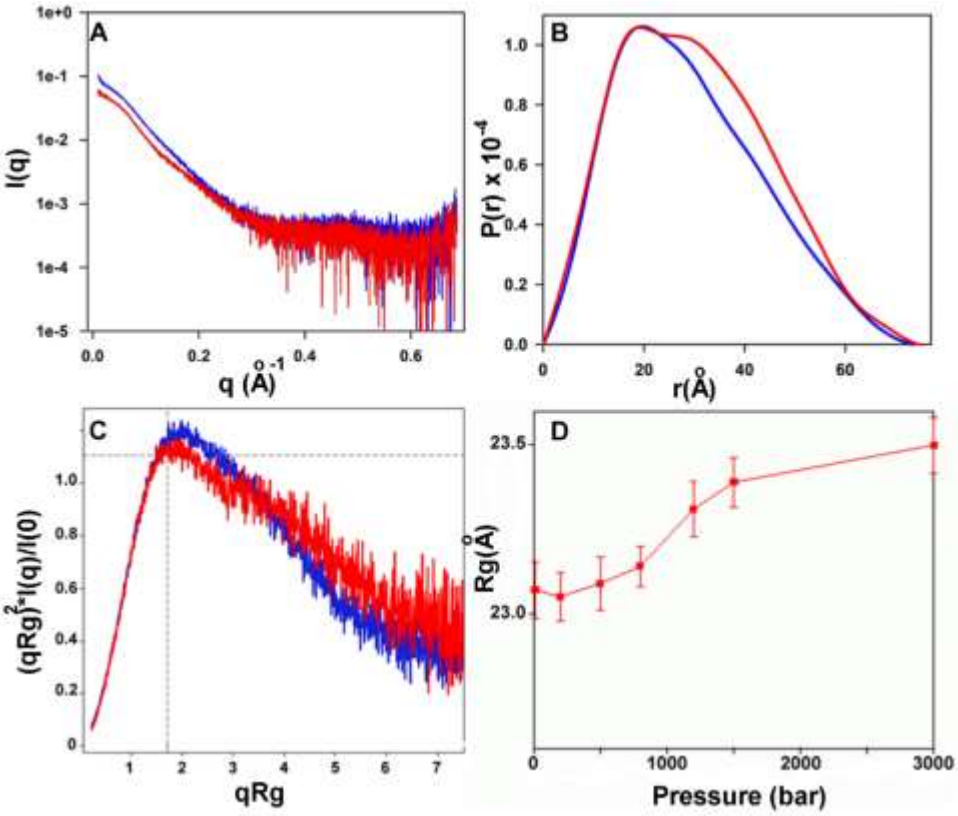

Figure 3. Effect of pressure on the SAXS profiles of tRNA^{Lys3}. A) SAXS intensity profiles, B) Pair distance distribution (P(r)) plots, C) Normalized Kratky plots and D) Pressure dependence of the radius of gyration (R_g) calculated from the P(r) profiles. Blue – 10 bar; red 3000 bar.

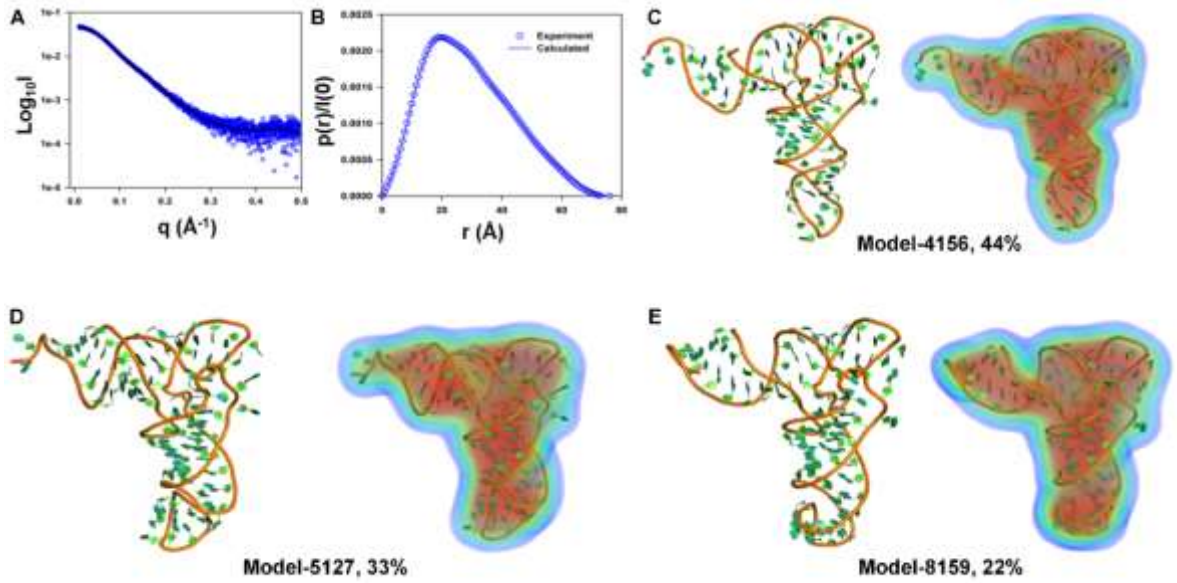

Figure 4. Ensemble Optimization of tRNALys3 at 10 bar. A) SAXS intensity profile and B) P(r) distribution with experimental results (open blue circles) with the fit from EOM (black (A) or blue (B) line) optimization resulting in the three configurations in C-E). C-E) The three models that best describe the SAXS profiles recovered from EOM as described in the Methods section labeled for the configuration number and relative population in the final fitted ensemble. For each configuration the cartoon structure with orange backbone and green filled bases (left) and the electron density (right) calculated using Chimera (ref). Red is highest density, blue is lowest. The structure on the left is fitted in the electron density using Chimera.

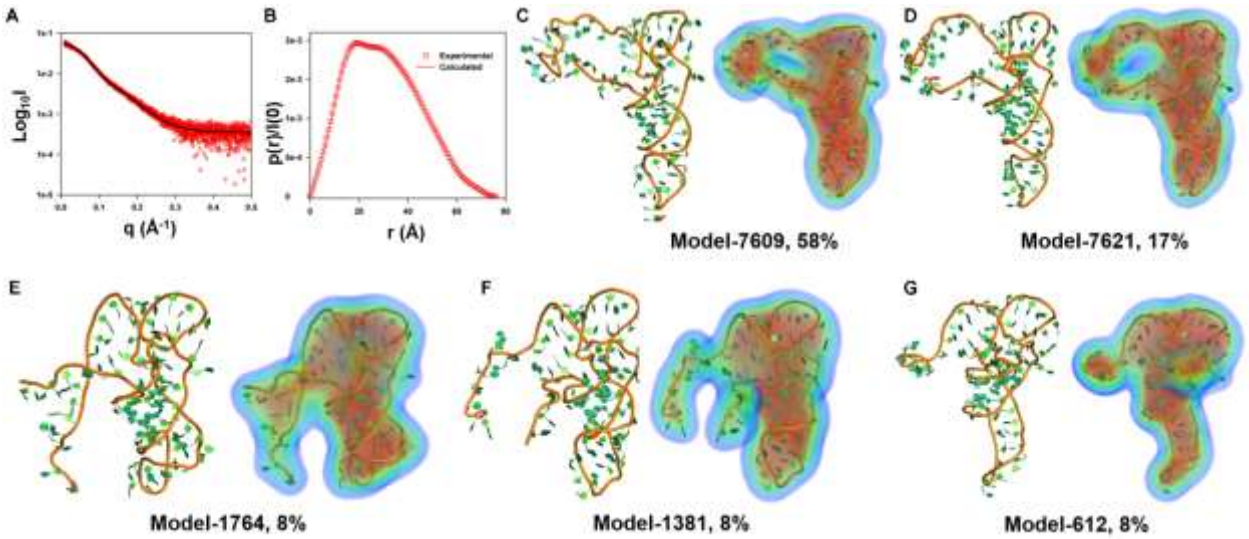

Figure 5. Ensemble Optimization of tRNALys3 at 3000 bar. A) SAXS intensity profile and B) P(r) distribution with experimental results (open red circles) with the fit from EOM (black or red line) with the five configurations in C-G). C-F) The five models that best describe the SAXS profiles recovered from EOM as described in the Methods section labeled for the configuration number and relative population in the final fitted ensemble. For each configuration the cartoon structure with orange backbone and green filled bases (left) and the electron density (right) calculated using Chimera (95). Red is highest density, blue is lowest. The structure on the left is fitted in the electron density using Chimera.

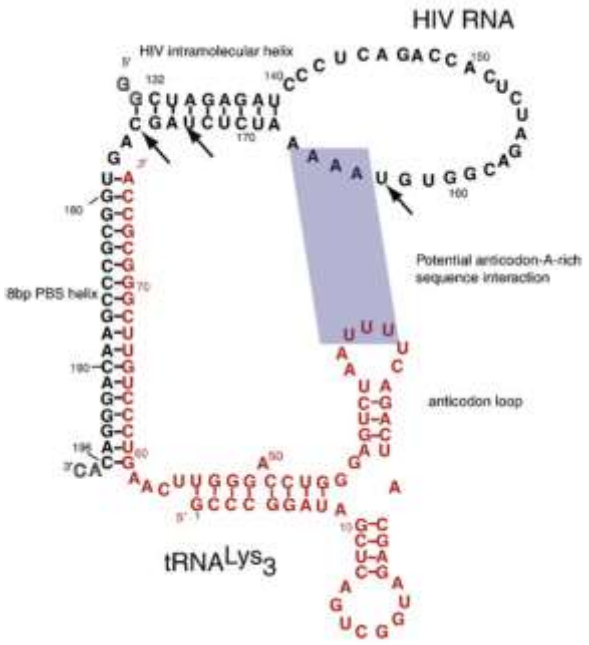

Figure 6. Secondary structure of the tRNALys3-HIV initiation complex. The secondary structure represented in this figure was previously determined by NMR (49) and is reproduced here.